Published on 28 September 2020. Downloaded by National Institutes of Standards & Technology on 10/13/2020 8:35:11 PM.

Soft Matter

PAPER

View Article Online
View Journal

Check for updates

Cite this: DOI: 10.1039/d0sm01566k

Observation of iron oxide nanoparticle synthesis in magnetogels using magnetic resonance imaging†

Samuel D. Oberdick,[ab] Stephen E. Russek,[a] Megan E. Poorman[a] and Gary Zabow*[a]

Received 30th August 2020,
Accepted 24th September 2020

DOI: 10.1039/d0sm01566k

rsc.li/soft-matter-journal

We show that magnetic resonance imaging (MRI) can be used to visualize the spatiotemporal dynamics of iron oxide nanoparticle growth within a hydrogel network during *in situ* coprecipitation. The synthesis creates a magnetic nanoparticle loaded polymer gel, or magnetogel. During *in situ* coprecipitation, iron oxide nanoparticles nucleate and grow due to diffusion of a precipitating agent throughout an iron precursor loaded polymer network. The creation of iron oxide particles changes the magnetic properties of the gel, allowing the synthesis to be monitored *via* magnetic measurements. Formation of iron oxide nanoparticles generates dark, or hypointense, contrast in gradient echo (GRE) images acquired by MRI, allowing nanoparticle nucleation to be tracked in both space and time. We show that the growth of iron oxide nanoparticles in the hydrogel scaffold is consistent with a simple reaction-diffusion model.

Introduction

Magnetite (Fe_3O_4) and maghemite (γ-Fe_2O_3) are widely researched for applications in materials science[1] and biomedicine[2] because of their robust magnetic properties and natural abundance. When combined with polymeric materials, these iron oxides can impart additional functionality by making the polymers magnetically responsive. These magnetic polymer composites, or magnetogels, have attracted interest for biomedical applications, particularly when remote actuation of flexible, porous materials is desirable.[3,4] For example, magnetogels have been used as remotely activated drug release agents, where oscillatory magnetic fields are used to enhance release of pharmaceutical agents from magnetically functionalized polymer networks.[5–8] Magnetogels have also been used to create flexible actuators and soft robots[9–12] enabling functions like swimming,[13] thermally induced shape change,[14] multimodal locomotion,[15] as well as jumping and gripping in origami inspired, 3D printed strucures.[16] Microparticles have also been fabricated from magnetogel composites and used as microscale magnetic barcode labels[17] and magnetic tweezers.[18]

While several methods have been developed for creating magnetic polymer composites, *in situ* coprecipitation has emerged as a preferred technique because of its ease and low cost. During this approach, a crosslinked polymer network is first soaked in an aqueous solution of iron salts, and then reacted with a precipitating agent (usually an alkali solution, such as NaOH or NH_4OH). The reaction proceeds as the precipitating agent diffuses through the polymer network, which causes nucleation and growth of iron oxide nanoparticles. The approach can be used to prepare stable iron oxide/polymer composites using a variety of gels with up to ~15% volume percentage of iron oxide.[19–22] The technique has also been used to create superparamagnetic nanochains and microparticles with saturation magnetization as high as 50% of bulk magnetite.[23,24]

The dynamics of *in situ* coprecipitation can be understood as a reaction-diffusion system.[25] The precipitating agent diffuses into the polymer network, where it reacts to form iron oxide. During the reaction, the precipitating agent is consumed, creating a time-dependent diffusion sink which can change the overall dynamics markedly from a system limited by diffusion alone. To optimize and scale *in situ* coprecipitation for materials science applications, it is important to establish techniques that can probe nanoparticle growth as a function of time. Here we show that MRI can be used to visualize the reaction-diffusion dynamics and determine effective diffusion rates using newly grown iron oxide nanoparticles.

While most often used for biomedical imaging and diagnosis, MRI can also be a powerful, noninvasive tool for visualizing chemical change in material systems. For instance, MRI has been used to explore complex material dynamics ranging from granular convection[26,27] to sap flow in plants,[28] and aging in stone structures or oil based artwork for preservation of cultural heritage.[29,30]

[a] Applied Physics Division, National Institute of Standards and Technology, Boulder, Colorado 80305, USA. E-mail: gary.zabow@nist.gov
[b] Department of Physics, University of Colorado, Boulder, Colorado 80309, USA

† Electronic supplementary information (ESI) available. See DOI: 10.1039/d0sm01566k

Published on 28 September 2020. Downloaded by National Institutes of Standards & Technology on 10/13/2020 8:35:11 PM.

The change in materials systems is most evident when chemical reactions are accompanied by creation or modification of MRI contrast. The high magnetic moment of iron oxide nanoparticles make them effective T_2 and T_2* MRI contrast agents because they generate magnetic field gradients, which dephase the proton-spin moments transverse to the polarizing B_0 field.[31] As such, MRI is ideally suited for observation of iron oxide nanoparticle growth. For example, radiologists regularly employ T_2* weighted imaging to track iron oxide growth and phase change in hemosiderin deposits when diagnosing cerebral microbleeds for traumatic brain injury.[32]

In this work, we demonstrate that newly synthesized iron oxide nanoparticles can be used as reporters for tracking reaction dynamics of *in situ* coprecipitation through MRI monitoring. We quantify the spatial reaction dynamics using gradient echo (GRE) imaging, which is particularly sensitive to hypointense contrast generation from magnetic nanoparticles. We show that the evolution of nanoparticle growth is consistent with a reaction-diffusion system where a precipitating agent diffuses through a polymer network. Finally, we show that the intrinsic properties of the polymer gel, such as porosity, can be correlated with nanoparticle size and used to understand magnetogel properties.

Experimental

Materials

Polyethylene glycol dimethacrylate (PEGDMA) was acquired from Polysciences Inc. with average molecular weights of 1000 and 8000 Dalton (PEGDMA 1000 and PEGDMA 8000). Iron chloride tetrahydrate, iron chloride hexahydrate, sodium hydroxide pellets and 2,2-dimethoxy-2-phenylacetophenone (DMPA) were purchased from Sigma Aldrich.

Hydrogel synthesis

Hydrogel composites were created using PEGDMA as a monomer and crosslinked using DMPA, an ultraviolet light sensitive photoinitiator. PEGDMA 1000 was heated above its melting point to 80 °C. Once the PEGDMA reached a liquid form, a 1% by weight solution of DMPA in PEGDMA was prepared and stored as stock. Hydrogel was cast by heating the DMPA/PEGDMA to 80 °C before it was poured into a mold. The hydrogel was cured under N_2 gas for 5 minutes using an ultraviolet lamp (365 nm). PEGDMA 8000 was prepared by dissolving PEGDMA 8000 monomer (initially in powder form) in a 25% weight solution of deionized water. Once dissolved, 1% by weight DMPA was dissolved in the subsequent solution. The resultant solution was crosslinked under inert N_2 gas for 5 minutes using an ultraviolet lamp (365 nm).

Magnetogel synthesis *via in situ* coprecipitation

Molded pieces of hydrogel were soaked in a solution of iron chlorides (2 : 1 ratio of Fe^{3+} to Fe^{2+}) for 24 hours. The swollen gel was removed from the solution of iron chlorides and submerged in 0.5 mol L^{-1} NaOH to initiate the coprecipitation reaction.

MRI experiments

MRI experiments were performed at 3 T using an Agilent preclinical scanner. Images were collected using gradient echo (GRE) sequences. Scan parameters for each experiment are listed in figure captions associated with each MRI experiment.

Magnetometry

Magnetometry measurements were performed using Quantum Design MPMS-7 and MPMS-3 magnetometers.

Transmission electron microscopy (TEM)

Magnetic nanoparticles were extracted from PEGDMA 1000 magnetogel for TEM by grinding the sample into a fine powder. The powder was mixed with oleic acid and toluene to stabilize free nanoparticles. Large pieces of the gel sedimented overnight and the supernatant was pipetted off. A small drop of this solution was dispensed *via* pipette on top of a carbon coated TEM grid acquired from Ted Pella. Imaging was done using a JEOL 2000-FX microscope.

Image analysis

MR images were analyzed using ImageJ.[33]

Results and discussion

In situ coprecipitation synthesis of magnetogels

This study focuses on magnetogels prepared using the method of *in situ* coprecipitation. Coprecipitation is a popular synthesis of magnetic nanoparticles because of its ease and use of relatively non-toxic precursors.[34] In general, coprecipitation refers to a process whereby metal salts are dissolved in water then mixed with a precipitating agent to form nanoparticles, usually made of metal oxides.[35] Typically, the synthesis is performed in aqueous solution and the precipitating agent is a strong base, such as NH_4OH or NaOH.[36] *In situ* coprecipitation, specifically, refers to a subset of coprecipitation syntheses which are used to grow nanoparticles within a medium besides aqueous solution. Here, we use *in situ* coprecipitation to grow iron oxide nanoparticles within crosslinked hydrogels. The final product is a magnetic nanoparticle/hydrogel composite, or a magnetogel. Fig. 1a shows a cartoon schematic of the process used to prepare magnetogels. A crosslinked hydrogel is first soaked in a bath of iron salts, prepared with a 2 : 1 ratio of Fe^{3+} to Fe^{2+}, so that ferrimagnetic Fe_3O_4 (Fe^{2+} $Fe^{3+}{}_2O_4$) is produced. Then, the hydrogel is transferred to a bath of basic solution (0.5 mol L^{-1} NaOH for all experiments in this manuscript). The base acts as a precipitating agent, nucleating and growing iron oxide nanoparticles as it diffuses through the gel.

Fig. 1b (top) Shows ~1 cm wide pieces of gel at various stages of a coprecipitation reaction. Initially, the crosslinked hydrogel is transparent. After being soaked in the bath of iron chlorides for ~24 hours, the gel develops a yellow color

 This journal is © The Royal Society of Chemistry 2020

Published on 28 September 2020. Downloaded by National Institutes of Standards & Technology on 10/13/2020 8:35:11 PM.

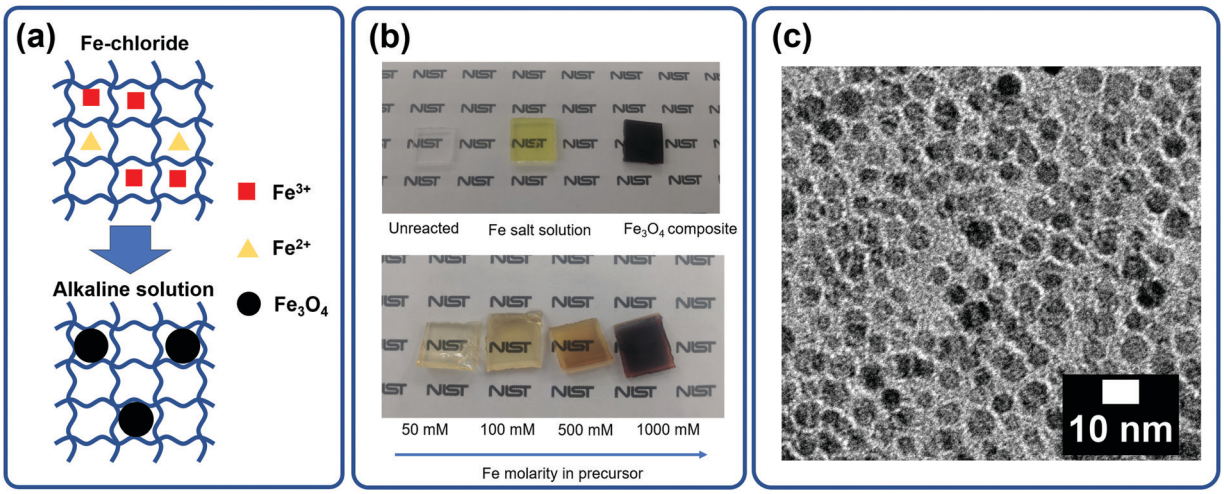

Fig. 1 (a) Cartoon schematic of the *in situ* coprecipitation process. A crosslinked hydrogel is soaked in a solution of iron chlorides then transferred to an alkaline solution, where iron oxide nanoparticles nucleate and grow. (b) Optical image of hydrogels in different stages of *in situ* coprecipitation (top) and reacted hydrogels with increasing molarity of elemental iron in the iron chlorides precursor (bottom). NIST logos are ~ 1 cm wide. (c) Transmission electron microscope (TEM) micrograph of ~6–7 nm iron oxide nanoparticles extracted from polymer matrix, following *in situ* coprecipitation.

uniformly across its face and throughout its interior. After sitting for 24 hours in a solution of 0.5 mol L^{-1} NaOH, the color of the gel changes from yellow to an opaque black, indicating that iron oxide has grown throughout the gel. The final density of iron oxide nanoparticles in the magnetogel can be tuned by varying the molarity of the iron chlorides in solution during the precursor soaking step. This can be seen in Fig. 1b (bottom), where the relative opacity of gels increases with the molarity of iron chlorides. Fig. 1c is a TEM micrograph of nanoparticles extracted from the magnetogel after synthesis. The particles are 6 nm to 7 nm and exhibit a spherical shape.

MRI of iron oxide growth during magnetogel synthesis

The magnetization of iron oxide particles generates MRI contrast, enabling regions of the gel laden with iron oxide particles to be distinguished from particle free regions. Iron oxide nanoparticles can locally shorten the T_2^* time, generating contrast in the resultant MR image. This contrast is especially apparent in GRE images, where dephasing from nanoparticles darkens the image. Fig. 2a and b show a comparison between optical and MR images of the same piece of hydrogel. *In situ* coprecipitation has been used to grow iron oxide nanoparticles selectively at either ends of a cylindrical slab of hydrogel, but not in the middle. A dark, or hypointense, contrast is observed in the gel where nanoparticles have been grown.

This MRI contrast generation allows tracking of iron oxide nanoparticle growth in a hydrogel network as a function of time. Fig. 3a shows a schematic of an experiment, where a cylindrical piece of hydrogel, previously soaked in iron chlorides (50 mmol L^{-1}, elemental iron in gel, 2 : 1 ratio of Fe^{3+} : Fe^{2+}), is submerged in a bath of NaOH (0.5 mol L^{-1}) and subsequently imaged in an MR scanner. At the start of the experiment (t = 0), the precipitating agent has yet to diffuse into the porous network and no iron oxide particles have nucleated. Some time later ($t > 0$), NaOH diffuses into the hydrogel starting at the

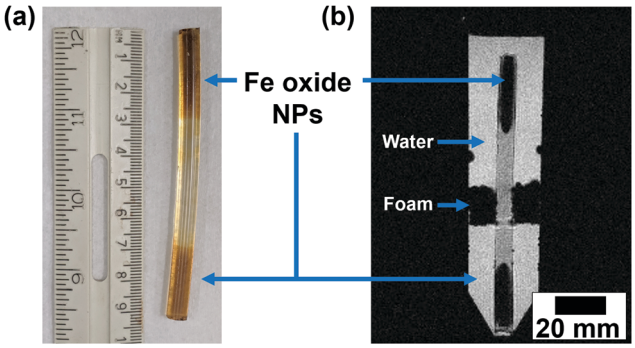

Fig. 2 (a) Optical image of hydrogel where *in situ* coprecipitation has been localized to the top and bottom of the polymer. (b) Corresponding MRI image collected using a GRE sequence (TE = 15 ms, TR = 120 ms, voxel size = 0.47 mm × 0.47 mm, slice thickness = 0.5 mm, flip angle = 20°). The polymer has been submerged in water and held in place with a foam support collar. Hypointense contrast is observed in regions of the gel where iron oxide nanoparticles have been grown within the polymer network.

hydrogel/NaOH bath interface. When a critical concentration of NaOH has permeated the hydrogel, iron oxide nanoparticles nucleate and grow in the polymer network. The generation of iron oxide perturbs local magnetic fields and magnetic field gradients, dephasing water proton spins and leading to the appearance of a hypointense contrast front. This can be clearly seen in the time series in Fig. 3b. After 11 664 s (3.24 h), the contrast of the hydrogel slab has transformed from light to dark, indicating that nanoparticles have grown throughout the gel.

To better quantify the evolution of the contrast, a similar experiment was repeated with higher spatial resolution. The length of the cylindrically symmetric hydrogel slab was extended so that it touched the bottom of the reaction tube (8 mm diameter and ~100 mm long). A region in the center of the gel was imaged so that diffusion from the top or bottom of

Published on 28 September 2020. Downloaded by National Institutes of Standards & Technology on 10/13/2020 8:35:11 PM.

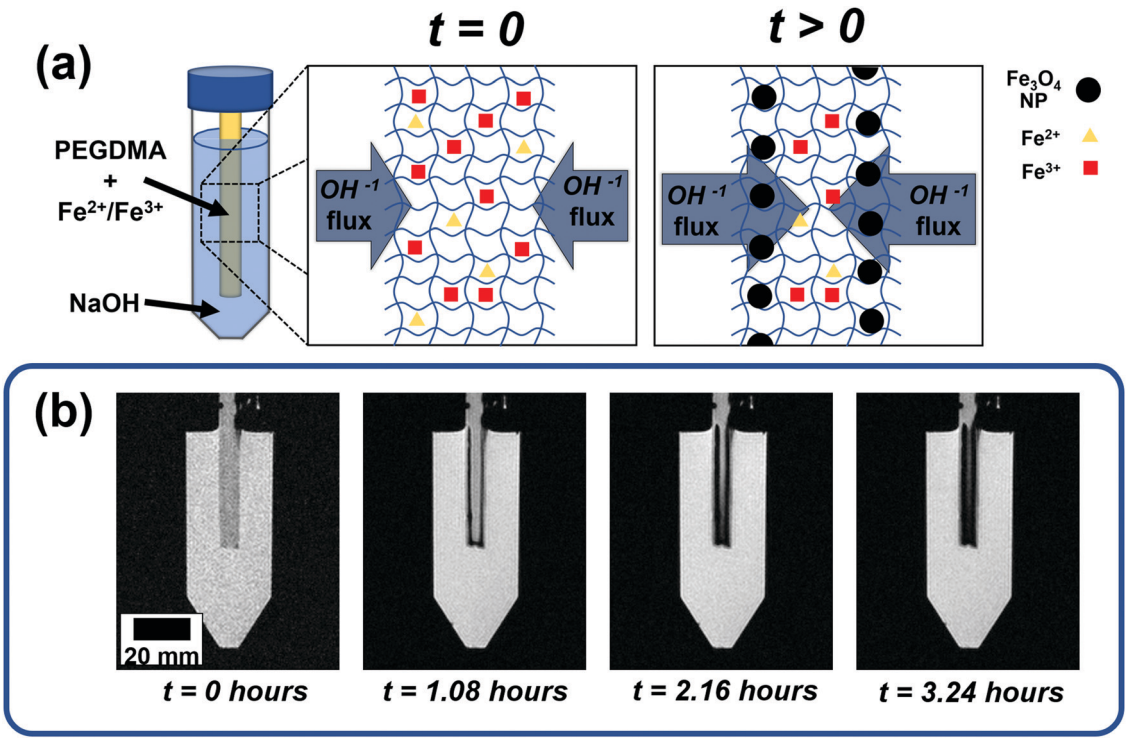

Fig. 3 (a) Cartoon schematic showing hydroxide diffusion driven dynamics of *in situ* coprecipitation reaction. (b) Time series of GRE images (TE = 15 ms, TR = 1000 ms, voxel size = 0.52 mm x 0.52 mm, slice thickness = 1 mm, flip angle = 15°) showing the progression of hypointense contrast caused by the nucleation and growth of iron oxide nanoparticles (50 mmol L^{-1} elemental iron in gel, 2 : 1 ratio of Fe^{3+} : Fe^{2+}).

the slab did not interfere with cylindrical symmetry. Fig. 4a–e display GRE images taken through the center of the cylindrical slab and show evolution of a hypointense contrast front originating at the hydrogel/NaOH interface and progressing inward over time. The experiment concludes at 10 304 s, at which point the interior contrast of the hydrogel has almost entirely changed. For each of the images, the total signal was integrated along the length of the cylinder, yielding an average signal as a function of cylinder radius. The integrated GRE signal was inverted so that the dark contrast front corresponded to a moving peak in the data. Fig. 4f–j shows the inverse, integrated signal intensity displayed as a function of distance across the image for corresponding GRE images in Fig. 4a–e.

Modelling and comparison to reaction-diffusion system

We compared the experimental data to a numerical model of reaction-diffusion driven *in situ* coprecipitation to better understand the system. Since the growing iron oxide tracks the penetration depth of the OH^{-1} ions into the gel, it is tempting to use such time-resolved image data directly to determine a diffusion coefficient for the mobile OH^{-1} ions. However, because the OH^{-1} ions are not only diffusing through the gel, but also simultaneously being removed when they come into contact and react with Fe^{2+} and Fe^{3+} cations (*via* the precipitation reaction that creates the iron oxide) the data cannot be fitted directly to a simple diffusion equation. Such a diffusion model would only be appropriate in the limit of an initial hydroxide concentration that vastly exceeds that of the iron ion concentration, such that any removal of hydroxide by the precipitation reaction is negligible (see ESI†). For the experiments presented here, however, we are not in that limit. The ratio of hydroxide to iron ions needed to generate magnetite (Fe_3O_4) can be estimated using the stoichiometrically balanced chemical reaction equation,

$$Fe^{+2} + 2Fe^{+3} + 8OH^- \xrightarrow{\text{yields}} Fe_3O_4 + 4H_2O. \quad (1)$$

The reaction stoichiometry requires a minimum initial number of hydroxide ions equal to 8/3 that of the net concentration of iron ions (Fe^{2+} and Fe^{3+}) if all the iron ions are to be converted into iron oxide. In the experiments this minimum is readily met with an initial OH^- concentration that is 10 times the net iron concentration. Moreover, this initial concentration is distributed over a volume 8 times the volume of the gel, located in the enclosed container. This means that there are at least 80 times the number of OH^- ions compared to iron ions. Despite the concentration of OH^- being many times higher than iron, our numerical simulation shows that the sink effect of OH^- reacting with Fe^{2+} and Fe^{3+} is not negligible.

For our experimental concentrations, the rate at which iron oxide forms through the gel becomes a complicated function of diffusion of hydroxide ions within gel microstructure, the initial concentration ratios of iron and hydroxide ions, coprecipitation reaction rate and the finite system geometry. Moreover, because the total amount of iron oxide created at any point in the gel is limited by iron cation concentration

 This journal is © The Royal Society of Chemistry 2020

Published on 28 September 2020. Downloaded by National Institutes of Standards & Technology on 10/13/2020 8:35:11 PM.

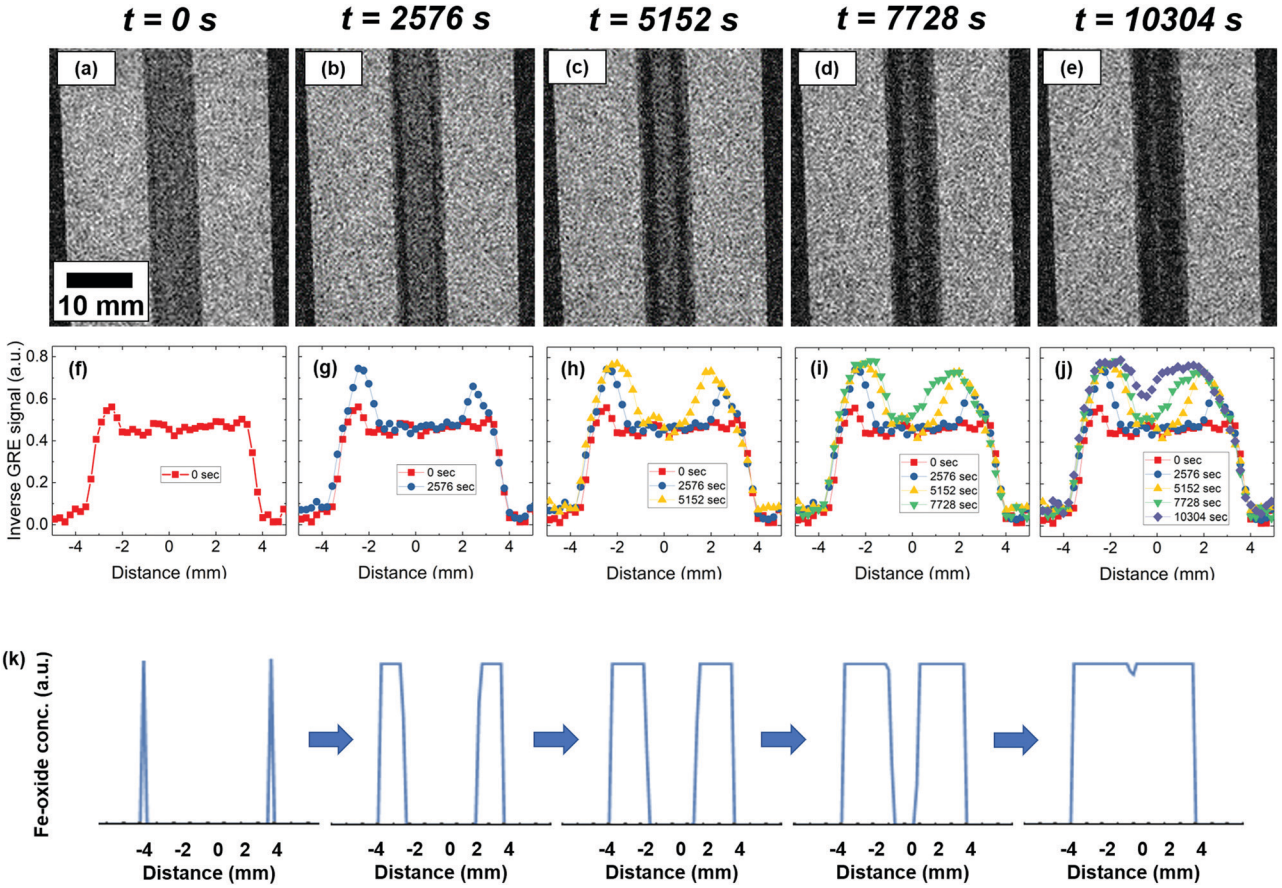

Fig. 4 (a–e) Time series of GRE images (TE = 5 ms, TR = 120 ms, voxel size = 0.26 mm × 0.26 mm, slice thickness = 0.7 mm, flip angle = 50°) showing hypointense contrast front moving in from either side of cylindrical hydrogel slab and advancing towards its center (25 mmol L^{-1} elemental iron in gel, 2 : 1 ratio of Fe^{3+} : Fe^{2+}). (f–j) Corresponding plots of the inverse intensity from GRE images, corrected for rotation and integrated across image, showing advancement of contrast front. (k) Reaction-diffusion simulation results showing iron oxide concentration in hydrogel cross section as a time series with times that roughly correspond to experimental data above (t = 50, 2500, 5000, 7500 and 10 000 seconds).

previously absorbed into the gel, the iron oxide nanoparticle growth front through the gel is not a smooth function. That is, the concentration of iron oxide is limited by the concentration of iron precursor and will saturate when all the precursor is consumed. No such saturation maximum applies to the OH^{-1} ions, however. This means that for these experiments, the concentration of precipitated iron oxide nanoparticles (the actual observable in MRI), is not proportional to the concentration of hydroxide ions.

Accurate modeling would require coupled reaction-diffusion equations that account not only for diffusive transport but also for the reaction, and removal, of the OH^{-1} ions during the *in situ* coprecipitation process. However, analytic evaluation of the diffusion constant for OH^{-1} ions is further complicated by the finite capacity of these effective sinks – once the iron precursor at any particular location has been converted to iron oxide, there is no longer any sink for OH^{-1} at that location. Because of these complications, we choose to model the diffusion-reaction numerically.

The model allows hydroxide ions to diffuse *via* a first principles Monte Carlo process at each time step. When hydroxide and iron precursor encounter one another, they are eliminated to form iron oxide (in ratios determined by stoichiometry in eqn (1)). The diffusion rate is set by picking a diffusion coefficient for the hydroxide ions within the hydrogel, D_{OH}. Note that D_{OH} is the only free variable used in matching the simulation to the experiment (see ESI†).

By matching how long it takes the simulated model to grow iron oxide throughout the gel to the experimental times observed in the MRI data, we can determine $D_{OH} = 4 \times 10^{-10}$. The results from the simulation are compared to experiment in Fig. 4k. The simulation also captures qualitative aspects of the experimental data, such as the sharp profile of the moving iron oxide front. It should be noted that, while MRI is often used to measure diffusion through porous media, here the iron oxide creation leads to a continually changing magnetic field environment. This interferes with the local magnetic field gradient control needed for standard MRI pulse schemes that measure diffusion, which limits the applicability of standard MRI diffusion measurements in such magnetogel systems.

Also, the above analysis assumes that the diffusion coefficient is constant throughout the reaction. In the regime where newly created iron oxide nanoparticles occupy a significant volume fraction of the magnetogel, it is unlikely that the coefficient of

Published on 28 September 2020. Downloaded by National Institutes of Standards & Technology on 10/13/2020 8:35:11 PM.

diffusion is constant since the particles themselves would obstruct further diffusion. For the experiments performed here, however, the final volume fraction of iron oxide particles, φ, is low enough that we do not expect the effective coefficient of diffusion to be impacted significantly ($\varphi \sim 0.00007$ or $\sim 0.007\%$, calculation in ESI†).

Relationships between porosity of gel and magnetogel synthesis and properties

The numerical estimate of hydroxide diffusion above can be compared to polymer model calculations of hydroxide diffusion within a hydrogel network. The reduction of diffusion coefficient from free water to the gel can be correlated with the porosity of the hydrogel used in the experiment. We calculated the linear mesh size, ξ, of PEGDMA 1000, defined as the average linear distance between crosslinks, and found it to be $\xi \sim 3$ nm (ESI†). The mesh size can be used to calculate to ratio of D_{gel}/D_0 or the ratio of the coefficient of diffusion within the gel *versus* outside,[37]

$$\frac{D_{gel}}{D_0} = \left(1 - \frac{r_S}{\xi}\right) \exp\left\{-Y\left(\frac{v_{2,s}}{1 - v_{2,s}}\right)\right\} \quad (2)$$

where r_s is the hydrodynamic radius of the solute (0.11 nm for OH^{-1}),[38] Y is critical volume parameter (taken as 1 for PEG based gels),[37] and $v_{2,s}$ is the volume fraction occupied by polymer (0.58 for this system, calculation in ESI†).[39] Evaluating eqn (2) with the parameters for PEGDMA gives $D_{gel}/D_0 \sim 0.24$ and $D_{gel} \sim 1 \times 10^{-9}$ m^2 s^{-1}. This order-of-magnitude calculation predicts a reduced diffusion in fair agreement with the diffusion coefficient estimated from MRI data ($D_{OH} \sim 4 \times 10^{-10}$ m^2 s^{-1}).

Finally, magnetometry was used to characterize the iron oxide nanoparticles embedded in the hydrogel following completion of *in situ* coprecipitation. Fig. 5a shows a plot of the (mass) magnetization, M_s, as a function of applied magnetic field taken at a temperature of 300 K for a piece of magnetogel prepared using 100 mmol L^{-1} of elemental iron (2 : 1 Fe^{3+} : Fe^{2+}). The data shows the characteristic, Langevin curve form attributed to superparamagnetic particles. The curve was fit to a single Langevin function,

$$M(\alpha H) = M_o\left(\coth(\alpha H) - \frac{1}{\alpha H}\right);\ \alpha = \frac{\mu}{k_B T} = \frac{M_s V}{k_B T} \quad (3)$$

where M_o is the saturation magnetization of the composite, H is the applied field, k_BT is product of Boltzmann's constant and temperature, and μ is the magnetic moment of a single particle. An estimate of the diameter of the iron oxide nanoparticles was extracted from the fit, assuming that $\mu = M_S V$ with spherical volume of particles and a saturation magnetization matching bulk magnetite (M_S = 480 kA m^{-1}).[40] The diameter of particles using the Langevin fit was estimated to be ~ 6 nm.

The size of oxide particles grown in the hydrogel is related to the linear mesh size of the hydrogel, and ultimately affects stability of the final magnetogel. Following nucleation, the nanoparticles grow until they are sterically impeded by the hydrogel network surrounding them.[24] For this system, the particles grow to be larger than the mesh size (3 nm) but are constrained from growing further. Because the particles are larger than the characteristic pore size of the gel, it means that the nanoparticles cannot diffuse out of the network following nucleation and growth. Thus, the final magnetogel is stable in the sense that it will not leach nanoparticles over time. This has been confirmed by leaving magnetogel samples in water for months at a time, with no obvious color change of surrounding solution or observation of precipitant.

The interplay between particle size and mesh size of hydrogel was further investigated by comparing zero field cooled (ZFC) and field cooled (FC) curves from gels with different molecular weights. Fig. 5b shows ZFC/FC curves from magnetogel samples prepared using PEGDMA 1000 and 8000. Both were synthesized using the same molarity of iron chlorides precursor (100 mmol L^{-1} elemental iron in gel, 2 : 1 ratio of Fe^{3+} : Fe^{2+}). The peak in the ZFC curves shifts to a lower temperature as the molecular weight of the hydrogel monomer is reduced. This indicates that

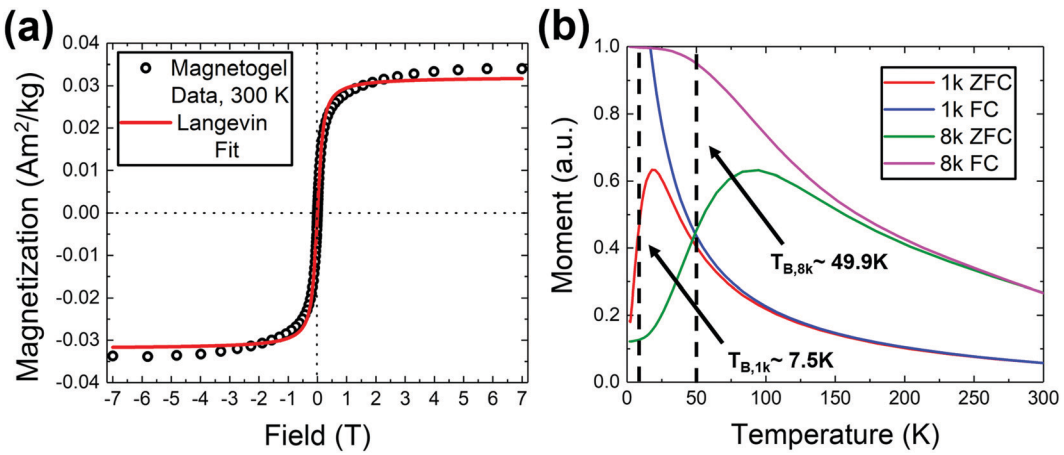

Fig. 5 (a) Magnetic moment as a function of field for a piece of magnetogel (diamagnetic background has been subtracted) and fit to Langevin function, normalized to mass of sample. (b) Zero field cooled (ZFC) and field cooled (FC) curves from magnetogel synthesized using PEGDMA with average molecular weight of 1000 and 8000 Da.

 This journal is © The Royal Society of Chemistry 2020

Published on 28 September 2020. Downloaded by National Institutes of Standards & Technology on 10/13/2020 8:35:11 PM.

the size of particles has been reduced, as well. To better quantify this size reduction, the blocking temperature was estimated from each curve and used to calculate an effective nanoparticle size. The blocking temperature of each curve was estimated using the inflection point to the left of the peak in the ZFC[41] instead of the peak in the ZFC. The diameter of iron oxide particles in the PEGDMA 1000 was calculated to be $\sim$6 nm, whereas the diameter of iron oxide nanoparticles in the PEGDMA 8000 was found to be $\sim$12 nm. This suggests that the diameter of iron oxide nanoparticles can be tuned by changing the hydrogel monomer's molecular weight.

Discussion

The experiments described in this manuscript show that MRI can be used to track changing magnetic properties of magnetogels during synthesis. By relating the evolution of nanoparticle growth to reaction-diffusion phenomena, this research also provides a framework for understanding *in situ* coprecipitation formation of magnetogels. This basic understanding is important for situations where researchers may want to create magnetogels with shapes more complex than the cylindrical geometry described in the paper. Moreover, the basic visualization of diffusion fronts described here may inspire synthesis of more advanced, patterned magnetic structures by tuning pattern formation in diffusion-reaction phenomena in gels.[42,43]

Conclusions

In conclusion, we have demonstrated that MRI enables observation of iron oxide nanoparticle growth during *in situ* coprecipitation based syntheses of magnetogel composites. Contrast generation in MRI can be used to quantify spatiotemporal characteristics of iron oxide formation. We related the reaction-diffusion dynamics of *in situ* coprecipitation to the moving front of iron oxide growth in the gel. Finally, we show that the porosity of gels is correlated with the diameter of iron oxide nanoparticles and the rate of the diffusion-reaction system.

Conflicts of interest

There are no conflicts to declare.

Acknowledgements

S. D. O. would like to acknowledge helpful discussions about MRI with Kathryn Keenan (NIST). S. D. O. and M. E. P. acknowledge support provided by an NRC Postdoctoral Fellowship. This work was performed under the following financial assistance award 70NANB18H006 from U.S. Department of Commerce, National Institute of Standards and Technology. Any mention of commercial products is intended solely for fully detailing experiments; it does not imply recommendation or endorsement by NIST.

References

1 R. Dronskowski, The Little Maghemite Story: A Classic Functional Material, *Adv. Funct. Mater.*, 2001, **11**, 27–29.
2 K. M. Krishnan, Biomedical Nanomagnetics: A Spin Through Possibilities in Imaging, Diagnostics, and Therapy, *IEEE Trans. Magn.*, 2010, **46**, 2523–2558.
3 S. R. S. Veloso, P. M. T. Ferreira, J. A. Martins, P. J. G. Coutinho and E. M. S. Castanheira, Magnetogels: Prospects and Main Challenges in Biomedical Applications, *Pharmaceutics*, 2018, **10**, 145.
4 Y. Li, *et al.*, Magnetic Hydrogels and Their Potential Biomedical Applications, *Adv. Funct. Mater.*, 2013, **23**, 660–672.
5 X. Zhao, *et al.*, Active scaffolds for on-demand drug and cell delivery, *Proc. Natl. Acad. Sci. U. S. A.*, 2011, **108**, 67–72.
6 V. M. De Paoli, *et al.*, Effect of an Oscillating Magnetic Field on the Release Properties of Magnetic Collagen Gels, *Langmuir*, 2006, **22**, 5894–5899.
7 T.-Y. Liu, S.-H. Hu, T.-Y. Liu, D.-M. Liu and S.-Y. Chen, Magnetic-Sensitive Behavior of Intelligent Ferrogels for Controlled Release of Drug, *Langmuir*, 2006, **22**, 5974–5978.
8 R. Hernández, *et al.*, Magnetic Hydrogels Derived from Polysaccharides with Improved Specific Power Absorption: Potential Devices for Remotely Triggered Drug Delivery, *J. Phys. Chem. B*, 2010, **114**, 12002–12007.
9 S. R. Mishra, M. D. Dickey, O. D. Velev and J. B. Tracy, Selective and directional actuation of elastomer films using chained magnetic nanoparticles, *Nanoscale*, 2016, **8**, 1309–1313.
10 H. Banerjee, M. Suhail and H. Ren, Hydrogel Actuators and Sensors for Biomedical Soft Robots: Brief Overview with Impending Challenges, *Biomimetics*, 2018, **3**, 15.
11 M. M. Schmauch, S. R. Mishra, B. A. Evans, O. D. Velev and J. B. Tracy, Chained Iron Microparticles for Directionally Controlled Actuation of Soft Robots, *ACS Appl. Mater. Interfaces*, 2017, **9**, 11895–11901.
12 J. A.-C. Liu, J. H. Gillen, S. R. Mishra, B. A. Evans and J. B. Tracy, Photothermally and magnetically controlled reconfiguration of polymer composites for soft robotics, *Sci. Adv.*, 2019, **5**, eaaw2897.
13 H. Li, G. Go, S. Y. Ko, J.-O. Park and S. Park, Magnetic actuated pH-responsive hydrogel-based soft micro-robot for targeted drug delivery, *Smart Mater. Struct.*, 2016, **25**, 027001.
14 T. Weigel, R. Mohr and A. Lendlein, Investigation of parameters to achieve temperatures required to initiate the shape-memory effect of magnetic nanocomposites by inductive heating, *Smart Mater. Struct.*, 2009, **18**, 025011.
15 W. Hu, G. Z. Lum, M. Mastrangeli and M. Sitti, Small-scale soft-bodied robot with multimodal locomotion, *Nature*, 2018, **554**, 81–85.
16 Y. Kim, H. Yuk, R. Zhao, S. A. Chester and X. Zhao, Printing ferromagnetic domains for untethered fast-transforming soft materials, *Nature*, 2018, **558**, 274–279.
17 K. W. Bong, S. C. Chapin and P. S. Doyle, Magnetic Barcoded Hydrogel Microparticles for Multiplexed Detection, *Langmuir*, 2010, **26**, 8008–8014.

Published on 28 September 2020. Downloaded by National Institutes of Standards & Technology on 10/13/2020 8:35:11 PM.

18 S. K. Suh, S. C. Chapin, T. A. Hatton and P. S. Doyle, Synthesis of magnetic hydrogel microparticles for bioassays and tweezer manipulation in microwells, *Microfluid. Nanofluid.*, 2012, **13**, 665–674.
19 S. G. Starodubtsev, *et al.*, Formation of magnetite nanoparticles in poly(acrylamide) gels, *J. Phys. Condens. Matter.*, 2005, **17**, 1471–1480.
20 N. R. Nagireddy, *et al.*, Preparation and characterization of magnetic nanoparticles embedded in hydrogels for protein purification and metal extraction, *J. Polym. Res.*, 2011, **18**, 2285–2294.
21 Y. Wang, B. Li, Y. Zhou and D. Jia, Chitosan-induced synthesis of magnetite nanoparticles via iron ions assembly, *Polym. Adv. Technol.*, 2008, **19**, 1256–1261.
22 Y. Wang, B. Li, Y. Zhou, D. Jia and Y. Song, CS-Fe(II,III) complex as precursor for magnetite nanocrystal, *Polym. Adv. Technol.*, 2011, **22**, 1681–1684.
23 B. Li, D. Jia, Y. Zhou, Q. Hu and W. Cai, In situ hybridization to chitosan/magnetite nanocomposite induced by the magnetic field, *J. Magn. Magn. Mater.*, 2006, **306**, 223–227.
24 S. K. Suh, *et al.*, Synthesis of Nonspherical Superparamagnetic Particles: In Situ Coprecipitation of Magnetic Nanoparticles in Microgels Prepared by Stop-Flow Lithography, *J. Am. Chem. Soc.*, 2012, **134**, 7337–7343.
25 H. K. Henisch, *Crystals in Gels and Liesegang Rings*, Cambridge University Press, 2005.
26 E. E. Ehrichs, *et al.*, Granular Convection Observed by Magnetic Resonance Imaging, *Science*, 1995, **267**, 1632–1634.
27 A. Penn, *et al.*, Real-time probing of granular dynamics with magnetic resonance, *Sci. Adv.*, 2017, **3**, e1701879.
28 T. W. J. Scheenen, F. J. Vergeldt, A. M. Heemskerk and H. V. As, Intact Plant Magnetic Resonance Imaging to Study Dynamics in Long-Distance Sap Flow and Flow-Conducting Surface Area, *Plant Physiol.*, 2007, **144**, 1157–1165.
29 E. Danieli and B. Blümich, Single-sided magnetic resonance profiling in biological and materials science, *J. Magn. Reson.*, 2013, **229**, 142–154.
30 N. Proietti, D. Capitani and V. Di Tullio, Applications of Nuclear Magnetic Resonance Sensors to Cultural Heritage, *Sensors*, 2014, **14**, 6977–6997.
31 H. B. Na, I. C. Song and T. Hyeon, Inorganic Nanoparticles for MRI Contrast Agents, *Adv. Mater.*, 2009, **21**, 2133–2148.
32 S. Haller, *et al.*, Cerebral Microbleeds: Imaging and Clinical Significance, *Radiology*, 2018, **287**, 11–28.
33 C. A. Schneider, W. S. Rasband and K. W. Eliceiri, NIH Image to ImageJ: 25 years of image analysis, *Nat. Methods*, 2012, **9**, 671–675.
34 T. Ahn, J. H. Kim, H.-M. Yang, J. W. Lee and J.-D. Kim, Formation Pathways of Magnetite Nanoparticles by Coprecipitation Method, *J. Phys. Chem. C*, 2012, **116**, 6069–6076.
35 R. Qiao, C. Yang and M. Gao, Superparamagnetic iron oxide nanoparticles: from preparations to in vivo MRI applications, *J. Mater. Chem.*, 2009, **19**, 6274–6293.
36 R. Massart, Preparation of aqueous magnetic liquids in alkaline and acidic media, *IEEE Trans. Magn.*, 1981, **17**, 1247–1248.
37 S. R. Lustig and N. A. Peppas, Solute diffusion in swollen membranes. IX. Scaling laws for solute diffusion in gels, *J. Appl. Polym. Sci.*, 1988, **36**, 735–747.
38 Y. Marcus, Volumes of aqueous hydrogen and hydroxide ions at 0 to 200 °C, *J. Chem. Phys.*, 2012, **137**, 154501.
39 B. Amsden, Solute Diffusion within Hydrogels. Mechanisms and Models, *Macromolecules*, 1998, **31**, 8382–8395.
40 B. D. Cullity and C. D. Graham, *Introduction to Magnetic Materials*, John Wiley & Sons, 2011.
41 K. L. Livesey, *et al.*, Beyond the blocking model to fit nanoparticle ZFC/FC magnetisation curves, *Sci. Rep.*, 2018, **8**, 11166.
42 H. Nabika, M. Itatani and I. Lagzi, Pattern Formation in Precipitation Reactions: The Liesegang Phenomenon, *Langmuir*, 2020, **36**, 481–497.
43 K.-J. Lee, W. D. McCormick, J. E. Pearson and H. L. Swinney, Experimental observation of self-replicating spots in a reaction–diffusion system, *Nature*, 1994, **369**, 215–218.

 This journal is © The Royal Society of Chemistry 2020